ISSN 1063-7737, Astronomy Letters, 2023, Vol. 49, No. 11, pp. 699–713. © Pleiades Publishing, Inc., 2023.
Russian Text © The Author(s), 2023, published in Pis'ma v Astronomicheskii Zhurnal, 2023, Vol. 49, No. 11, pp. 780–794.

Nature of the Eclipsing Polar 1RXS J184542.4+483134

V. Yu. Kochkina[1,2*], A. I. Kolbin[1,2,3], N. V. Borisov[1], and I. F. Bikmaev[2]**

[1] *Special Astrophysical Observatory, Russian Academy of Sciences, Nizhnii Arkhyz, Karachai-Cherkessian Republic, 357147 Russia*

[2] *Kazan (Volga Region) Federal University, Kazan, 420000 Russia*

[3] *North-Caucasus Federal University, Stavropol, 355017 Russia*

Received October 5, 2023; revised November 16, 2023; accepted November 16, 2023

Abstract—We have carried out a comprehensive study of the poorly investigated eclipsing polar 1RXS J184542.4+483134 with a short orbital period $P_{orb} \approx 79$ min. An analysis of its long-term light curves points to a change in the position and sizes of the accretion spot as the accretion rate changes. Narrow and broad components, which are probably formed on the ballistic segment of the accretion stream and on the magnetic trajectory, respectively, are identified in the emission line profiles. An inversion of the line profiles from emission to absorption due to the obscuration of the accretion spot by the accretion stream is observed. Based on the eclipse duration and the radial velocities of the narrow line component, we impose constraints on the white dwarf mass, $0.49 \leq M_1/M_\odot \leq 0.89$, and the orbital inclination, $79.7^\circ \leq i \leq 84.3^\circ$. An analysis of the cyclotron spectra points to the presence of two accretion spots with magnetic field strengths $B_1 = 28.4^{+0.1}_{-0.2}$ MG and $B_2 = 30 - 36$ MG. The main spot has a complex structure that apparently has a dense core and a less dense periphery emitting a spectrum with cyclotron harmonics. Polarization observations reveal a circular polarization sign reversal during the orbital period and an anticorrelation of the polarization with the brightness of the polar. Our modeling of polarization observations using the simple model of an accreting white dwarf shows that the polarization properties can be interpreted in terms of two-pole accretion with different optical depths of the accretion spots ($\tau_1/\tau_2 \sim 10$). An analysis of the Swift/XRT observations points to a predominance of bremsstrahlung in the X-ray radiation from the system.

DOI: 10.1134/S1063773723110051

Keywords: *stars: novae, cataclysmic variables; individual: 1RXS J184542.4+483134; methods: photometry, polarimetry, spectroscopy.*

1. INTRODUCTION

Cataclysmic variables are close binary systems that consist of a white dwarf (primary) and a cool G–L dwarf (secondary) filling its Roche lobe (Warner 1995). The material of the secondary outflows from the vicinity of the Lagrange point L_1 and, in the absence of a strong white dwarf magnetic field ($B \lesssim 0.1$ MG), forms an accretion disk. A different picture of accretion is observed in the case of strong white dwarf magnetization ($B \sim 10$–200 MG), which takes place in representatives of a subclass of cataclysmic variables called polars or AM Her stars (Cropper 1990). In such systems the material ejected by the secondary rapidly reaches the threading region, where the ram pressure of the gas stream becomes equal to the white dwarf magnetic pressure ($\rho v^2 = B^2/8\pi$). Thereafter, the ionized gas of the stream moves along magnetic field lines toward the magnetic poles of the white dwarf. When the infalling gas interacts with the stellar surface, a shock front is formed, after which the gas is heated to temperatures $T \sim 10$–50 keV (Aizu 1973). Subsequently, the material settles to the stellar surface, cooling through X-ray bremsstrahlung and optical cyclotron radiation. The height of the shock front is often smaller than its extent along the stellar surface due to the high gas cooling efficiency, and the shock structures are called accretion spots. The strong magnetic field of polars leads to synchronization of the white dwarf rotation with its orbital motion. A study of polars is important for understanding the generation and structure of the magnetic fields of white dwarfs (Ferrario et al. 2015; Briggs et al. 2018). Another interesting aspect in studying AM Her systems is related to the influence of magnetic fields on the evolution of close binary

*E-mail: nikainspace@gmail.com
**E-mail: kolbinalexander@mail.ru

systems (Belloni et al. 2020). In addition, polars are natural laboratories for studying the interaction of a supersonic plasma with stellar magnetospheres (Hameury et al. 1986; Li 1999) and understanding the accretion under conditions of strong magnetic fields (Busschaert et al. 2015; Bonnet-Bidaud et al. 2015).

In the optical range polars are distinguished by a great variety of observational properties. Because of the high contribution of the cyclotron component to the radiation from the system, polars are strongly polarized sources ($\sim$10–30%) (Tapia 1977), and cyclotron line harmonics often manifest themselves in their spectra (see, e.g., Rousseau et al. 1996). Accretion stream photoionization gives rise to intense hydrogen, HeI, and HeII λ4686 emission lines (Schwope et al. 1997). High and low states differing in mean brightness by several magnitudes are identified in the long-term light curves. The state change occurs due to the change in the rate of mass transfer from the secondary (Hessman et al. 2000).

This paper is devoted to investigating the poorly studied polar 1RXS J184542.4+483134 (hereafter J1845). It was identified by Denisenko and Sokolovsky (2011) as a cataclysmic variable. Based on their analysis of X-ray, ultraviolet, and optical observations, Pavlenko et al. (2011) classified J1845 as an eclipsing polar with an orbital period $P_{\rm orb} \approx 0.054908$ day ($\approx$79 min). This period is close to the minimum period of a cataclysmic variable, $P_{\rm min} \approx$ 80 min, at which the characteristic donor mass loss time becomes equal to the thermal one. Near the period $P_{\rm min}$ the evolution of the system changes from a decreasing period to an increasing one (McAllister et al. 2019; Knigge et al. 2011). The magnetic nature of J1845 was confirmed by Borisov et al. (2016a, 2016b), who detected a circular polarization changing from -10 to 30% during the orbital period. The polarization in this case anticorrelated with the brightness of the star.

In this paper we carried out a comprehensive optical study of J1845 including the analysis of phase-resolved spectroscopy, photometry, and photopolarimetry. In the next section we describe the optical observations of J1845 and the data reduction. Then, in section 3, we analyze the photometry for J1845. Section 4 is devoted to the orbital behavior of emission lines. Then, in section 5 we constrain the masses of the system components and the orbital inclination. In section 6 we analyze the cyclotron spectra and determine the magnetic field strength in the accretion spots. In section 7 we interpret the polarization observations and reconstruct the positions of the accretion spots on the white dwarf surface. The Swift X-ray and ultraviolet observations are analyzed in section 8. In the Conclusions we summarize our results.

2. OBSERVATIONS AND DATA REDUCTION

2.1. Spectroscopy

A set of spectra for the polar J1845 was taken with the 6-m BTA telescope at the Special Astrophysical Observatory of the Russian Academy of Sciences on the nights from September 21 to 22, 2011, and from April 28 to 29, 2012. On the first night the telescope was equipped with the SCORPIO-2 focal reducer (Afanasiev and Moiseev 2011) in the long-slit spectroscopy mode.[1] A 2 K $\times$ 2 K E2V CCD42-90 CCD array and a volume phase holographic grating, VPHG1200@540 (1200 lines/mm), which covered the range $\lambda\lambda = 3650-7250$ Å with an effective spectral resolution $\Delta\lambda \approx 5.2$ Å at a slit width of $0.96''$, were used in the instrument. We took a total of 22 spectra with exposure times of 300 s covering $\approx$1.5 orbital periods of the polar. On the second night, April 28/29, 2012, long-slit spectra were taken with the SCORPIO-1 focal reducer[2] equipped with a 2K×2K EEV CCD42-40 CCD array and VPHG1200G. We took 25 spectra with exposure times of 300 s covering $\approx$1.5 periods of J1845. The spectra covered the range $\lambda\lambda = 3900-5700$ Å with a resolution $\Delta\lambda \approx 5$ Å at a slit width of $1''$. All our observations were carried out in good astroclimatic conditions with a seeing of $1.0''$ and $1.5''$ in 2011 and 2012, respectively.

The spectroscopic data were reduced using the IRAF software package.[3] The spectral frames were bias subtracted, and the cosmic-ray hits were removed using the LaCosmic algorithm (van Dokkum 2001). A correction for the CCD sensitivity microvariations was made based on flat-field lamp frames. We corrected the geometric distortions and calibrated the spectra in wavelengths using calibration He-Ne-Ar lamp frames. An optimal extraction of the spectra (Horne 1986) with sky background subtraction was performed. We carried out spectrophotometric calibration based on the observations of the standard stars G191-B2B (Oke 1990) in 2011 and BD 33° 2642 (Bohlin et al. 1995) in 2012. For each spectrum we calculated the barycentric Julian dates and the barycentric corrections to the radial velocity.

[1] For more details on the SCORPIO-2 focal reducer, see https://www.sao.ru/hq/lsfvo/devices/scorpio-2/index.html.

[2] For more details on the SCORPIO focal reducer, see https://www.sao.ru/hq/lsfvo/devices/scorpio/scorpio.html.

[3] The IRAF astronomical data processing and analysis package was developed by the National Optical Astronomy Observatory (USA) and is accessible at https://iraf-community.github.io.

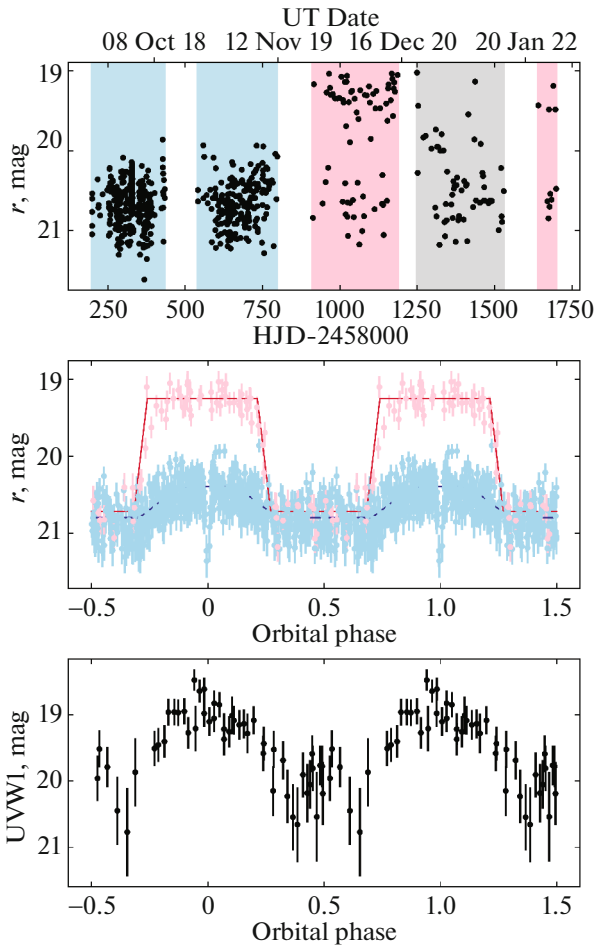

Fig. 1. Upper panel: the long-term light curve of J1845 from ZTF data in the r band. The data in the blue and pink regions correspond to the low and high states, respectively, while the segment in the gray region is difficult to classify by state. The middle panel: the r-band phased light curves in the low (blue dots) and high (pink dots) states fitted by trapezoids (solid lines). Lower panel: the Swift/UVOT light curve of J1845 in the UVW1 band.

2.2. Polarimetry

The photopolarimetric observations of J1845 were carried out on the nights from August 28 to 29, 2011, and from April 23 to 24, 2012, with the BTA telescope at the Special Astrophysical Observatory of the Russian Academy of Sciences using the SCORPIO-2 focal reducer equipped with an E2V CCD42-90 CCD array. A set of images for the neighborhood of J1845 was obtained in the V band of the Johnson system with exposure times of 30 and 120 s on the first and second nights, respectively. To analyze the polarization, we used a Wollaston prism with which the neighborhoods of J1845 were simultaneously imaged on the CCD array in the ordinary and extraordinary rays. To record the circular polarization, before the Wollaston prism we set a $\lambda/4$ phase plate rotated through 90° between the exposures to take into account the systematic errors.

The observational data were reduced in the IRAF package. The images were bias subtracted; the nonuniform CCD sensitivity was corrected based on flat-field images. The fluxes from J1845 in different polarization modes were determined by the method of aperture photometry. For details on the polarimetric measurements with SCORPIO-2 and their reduction, see Afanasiev and Amirkhanyan (2012).

2.3. Photometry at RTT-150

The photometric observations of J1845 were carried out on the nights of July 8/9 and July 13/14, 2022, with the Russian–Turkish 1.5-m telescope RTT-150 (TÜBİTAK National Observatory, Antalya, Turkey) using the TFOSC instrument in the photometer mode. The instrument is equipped with an ANDOR DZ936 BR DD, 2048 × 2048 pixel, CCD array thermoelectrically cooled to −80° C. The linear pixel size is 13.5 × 13.5 μm, corresponding to 0.33″ per pixel for 1 × 1 binning. The observations were carried out without using any photometric filters with 2 × 2 binning and a frame size of 1024 × 200 pixels to provide a time resolution ∼ 20 s. We took a total of 1002 frames at a seeing of 1.3 – 1.8″ (with exposure times of 15 s and a frame readout time of 3 s) covering ≈3.5 orbital periods of J1845. The CCD images were processed using the standard IRAF aperture photometry tools.

3. ANALYSIS OF PHOTOMETRY

Changes in the mean brightness reflecting the variability of the accretion rate are observed in the long-term photometric observations of polars. To analyze the long-term variability of J1845, we used data from the ZTF DR19 survey (Masci et al. 2019) spanning about four years. The largest volume of observational data for J1845 in this survey was obtained in the r band. The light curve of the polar in this band is shown in Fig. 1. It exhibits low and high states differing in maximum brightness by $\Delta r \approx 1^{\rm m}.5$.

The period $P_{\rm orb} = 79.06652 \pm 0.00025$ min was determined by the Lomb–Scargle method (VanderPlas 2018) based on the observations of J1845 in the low state. The phased light curves of J1845 in the low and high states are shown in Fig. 1. To construct them, we used the ephemeris

$$BJD_{\rm ecl} = 2459774.44506(6) + 0.0549072(2) \times E, \quad (1)$$

where the initial epoch corresponds to the mid-eclipse determined from the RTT-150 observations (see below).

The light curves in the two states have a bright phase extending approximately over half the orbital period ($0.70 \lesssim \varphi \lesssim 1.25$) and a dim phase ($0.25 \lesssim \varphi \lesssim 0.70$) the brightness in which changes little as the state changes. The bright phase is apparently formed during the passage of the accretion spot across the white dwarf disk, while the plateau phase corresponds to the time interval when the spot is behind the stellar disk. A shift of the bright phase and an increase in its duration during the transition from the low state to the high one are noticeable. To estimate the shift and extension of the bright phase, we fitted the segment of the light curves corresponding to it by trapezoids (see Fig. 1). It can be seen from a comparison of the fitting trapezoids that the bright phase in the high state occurs earlier by $\Delta\varphi = 0.07 \pm 0.04$ than in the low state, corresponding to an increase in the accretion spot longitude by $25^\circ \pm 14^\circ$ (if the longitude is measured in the direction of rotation of the white dwarf or, equivalently, in the direction of orbital motion of the donor). In addition, there is an increase in the duration of the bright phase by $\Delta\varphi = 0.12 \pm 0.08$, suggesting an extension of the accretion spot by $43^\circ \pm 29^\circ$ in longitude. These phenomena are apparently typical for polars and can be interpreted by the change in the position of the threading region caused by an increase in the ram pressure of the incoming gas during the transition from the low state to the high one (Schwope et al. 2015; Worpel and Schwope 2015; Kolbin et al. 2023).

An interesting feature of the presented light curves is that the brightnesses in the eclipse and the dim phase differ by no more than $0\overset{\text{m}}{.}2$. This behavior of the brightness is probably related to the partial eclipse of the white dwarf. Indeed, if the accretor surface does not contain the second bright spot, then the main emission source in the plateau phase must be the white dwarf. The brightnesses in the dim phase and the eclipse must be close in the case where the donor obscures a small part of the white dwarf disk containing the accretion spot. Another interpretation of this feature in the light curve of J1845 suggests the dominance of the donor emission over the white dwarf emission. In that case, the brightnesses in the eclipse and the plateau would also be equal. However, we think that this is unlikely due to the significant excess of the white dwarf brightness above the donor brightness in short-period ($P \sim 80$ min) cataclysmic variables.

The light curve of J1845 obtained with RTT-150 is shown in Fig. 2. The feature of J1845 noted above, i.e., the closeness of the brightnesses in the eclipse and the dim phase, is seen more clearly in it. The eclipse profile was fitted by a trapezoid. The eclipse duration was estimated from the width of the fitting trapezoid at half depth to be $\Delta t_{\text{ecl}} = 96.5 \pm 1.7$ s.

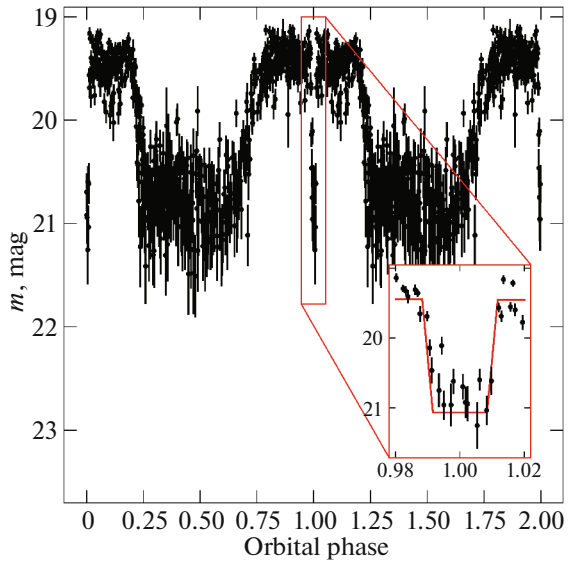

Fig. 2. The phased light curve of J1845 obtained with RTT-150 without using any photometric filters.

The eclipse depth was estimated to be $\Delta m = 1\overset{\text{m}}{.}62 \pm 0\overset{\text{m}}{.}18$. The presented errors in the parameters were found by the Monte Carlo method.

4. EMISSION LINES

The spectra of J1845 contain a set of emission lines typical for cataclysmic variables. The Hα, Hβ, Hγ Balmer lines, the HeI λ4921, λ5015, λ6678 lines, and the HeII λ4686 line are observed in the averaged spectrum. A multicomponent structure and a variability modulated with the orbital period are distinguished in the profiles of the strongest lines. The variability of the Hα profile is shown in the dynamic spectrum in Fig. 3. The behavior of other lines is similar but is less distinct due to the greater noisiness. In the range of phases $\varphi = 0.2 - 0.4$ the profile splits into two components: broad (FWHM ~ 870 km s^{-1}) and narrow (FWHM $\approx$440 km s^{-1}).

The behavior of the Hα profile components was analyzed by fitting them by the sum of two Gaussians:

$$f(v) = B + \sum_{i\in\{n,b\}} A_i \exp\left[-\frac{(v - V_i)^2}{2\sigma_i^2}\right], \qquad (2)$$

where v is the radial velocity of a point of the line profile, A is the height of the Gaussian, σ is the root-mean square deviation, V is the velocity of the Gaussian center, and B is the continuum level near the line (for a similar analysis of lines, see Liu et al. (2023) and Kolbin et al. (2023)). The indices n and b correspond to the narrow and broad components, respectively. We assumed a sinusoidal motion of the spectral profile components specified as

$$V_i = \gamma + K_i \sin\left[2\pi(\varphi - \varphi_i^0)\right], \qquad (3)$$

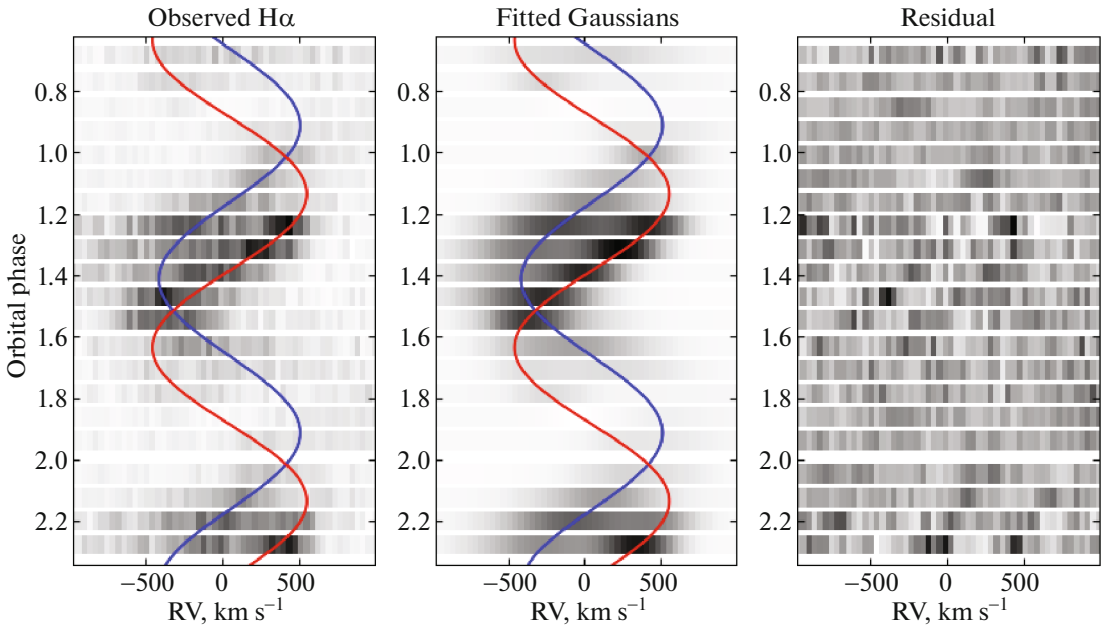

Fig. 3. The dynamic spectrum of the Hα line (left), the dynamic spectrum of the sum of the fitting Gaussians (center), and the residual dynamic spectrum (right) obtained by subtracting the fitting Gaussians from the observed spectra. The red and blue lines indicate the radial velocity curves of the narrow and broad components, respectively.

where $i \in \{n, b\}$, γ is the radial velocity of the system's center of mass, K is the radial velocity semi-amplitude, φ is the orbital phase, and φ^0 is the initial phase. The parameters γ, $K_{n,b}$, and $\varphi^0_{n,b}$ were determined by fitting the set of profiles by the least-squares method. The heights of the Gaussians $A_{n,b}$ and the continuum level B were found separately for each profile, while the parameters $\sigma_{n,b}$ were assumed to be time independent and were found by fitting the spectral profiles together with γ, $K_{n,b}$, and $\varphi^0_{n,b}$. The errors in the parameters were calculated by the Monte Carlo method. The reconstructed radial velocities of both components are shown in Fig. 3. For the narrow and broad components we found the radial velocity semi-amplitudes $K_n = 503 \pm 9$ km s^{-1} and $K_b = 447 \pm 12$ km s^{-1}, respectively. The difference of the initial phases for the two line components is $\Delta\varphi = 0.228 \pm 0.006$. Note that the emission line profiles for polars can have a fairly complex structure whose reproduction would require a larger number of components with changing widths (see, e.g., Schwope et al. 1997). However, since our observations are very noisy and the spectral resolution is low, the described fitting with two Gaussians turns out to be enough for a satisfactory description of the dynamic spectrum ($\chi^2_\nu \approx 1$).

The manifestation of a narrow emission component is a fairly common occurrence among polars (see, e.g., Schwope et al. 1997; Kolbin et al. 2022; Rodriguez et al. 2023). Its emergence is often associated with the effects of donor surface irradiation by the X-ray emission of the accretion spot. However, it is obvious from the radial velocity curve for the narrow component of J1845 that it is formed in a different region. Indeed, in the case of radiation from the donor surface, at phase $\varphi = 0.5$ the equality $V_n = \gamma$ would hold and a maximum flux in the narrow component would be reached, which is not observed for J1845.

The presented dynamic spectrum of the Hα line was used to reconstruct the Doppler tomogram, which is a map of the emission distribution in two-dimensional velocity space. Each point of this map can be specified by two polar coordinates: the absolute value of the velocity relative to the system's center of mass v (to within the factor $\sin i$, i is the orbital inclination) and the angle between the direction of the velocity vector of an emitting particle and the axis connecting the centers of mass of the stellar components ϑ. For more details on the interpretation of Doppler tomograms, see Marsh (2005) and Kotze et al. (2015, 2016). The Doppler maps were reconstructed using the doptomog-2.0 code, which implements the maximum entropy method (Kotze et al. 2015, 2016). The line flux changes during the orbital period of J1845, suggesting a high optical depth of the emitting region and/or its eclipses by the secondary. For this reason, we used the so-called flux-modulated version of Doppler tomography that suggests a sinusoidal change in the intensity

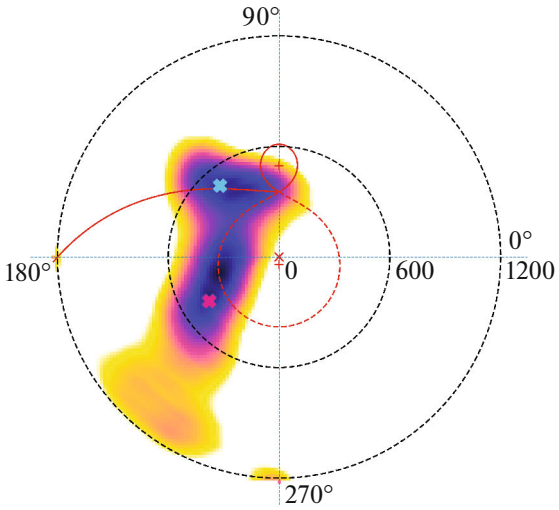

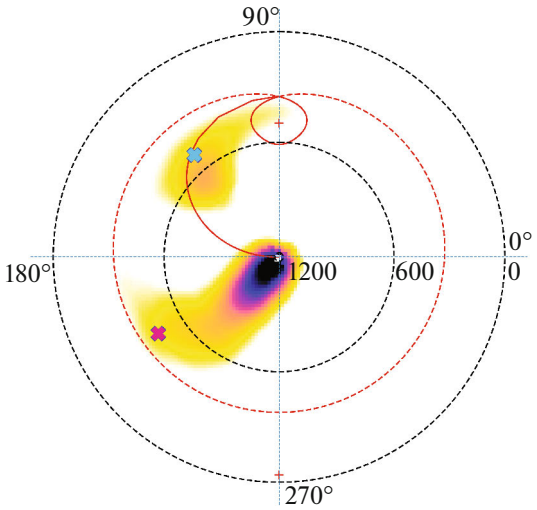

Fig. 4. Doppler tomograms of J1845 in the standard (top) and inside-out (bottom) projections. The blue and red crosses indicate the formation regions of the narrow and broad emission line components, respectively. The open red line indicate the particle velocities on the ballistic trajectory. The red closed and red dashed lines correspond to the Roche lobes of the donor and the white dwarf, respectively.

of the emission regions during the orbital period (Steeghs 2003).

Figure 4 shows the Doppler tomograms of J1845 in two projections: standard and inside-out. In the first projection the absolute value of the velocity v increases from the tomogram center to the periphery, while in the second one, on the contrary, it increases from the periphery to the center. The latter is convenient for investigating the high-velocity segments of the accretion stream that are strongly washed out on

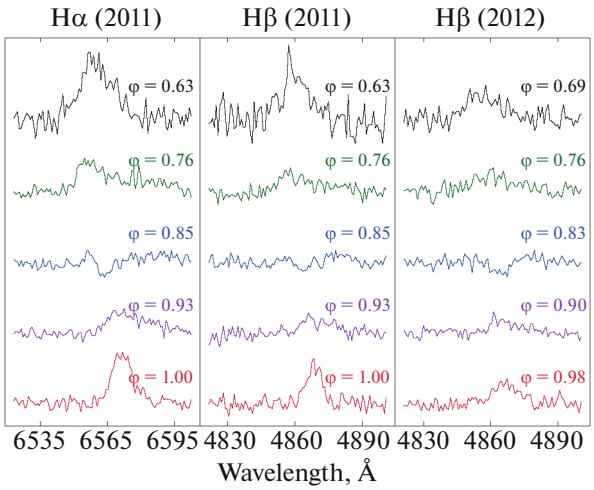

Fig. 5. Evolution of the Hα and Hβ profiles from the 2011 observations (two left panels) and the Hβ profile from the 2012 observations (right panel) near the orbital phase $\varphi = 0.85$. An inversion of the emission profile to the absorption one and back is obvious.

the maps in the standard projection (for more details on this effect, see Kotze et al. 2015). Two regions are observed on the tomograms: the first and the second correspond to the narrow and broad emission line components, respectively. The position of the source of the narrow component falls nicely on the trace of the ballistic trajectory calculated with parameters admissible for J1845 ($M_1 = 0.85\ M_\odot$, $M_2 = 0.07\ M_\odot$, and $i = 80°$; see the next section). The position of the broad component is consistent with the expected velocities of the accretion stream on the magnetic trajectory (Schwope et al. 1997). The angle ϑ is higher by $\sim 90°$ for the broad component than for the narrow one, apparently, due to the abrupt change in the direction of gas motion after the threading region. An extension of the formation region of the broad component in the direction of increase in the absolute value of the velocity v with increasing ϑ is noticeable. If the gas moves strictly along magnetic dipole lines, then this could point to a tilt of the dipole axis with respect to the white dwarf rotation axis.

An interesting feature in the behavior of spectral lines is the inversion of their profile from emission to absorption and back near the orbital phase $\varphi = 0.85$. This phenomenon is demonstrated in Fig. 5 for the Hα, Hβ, and HeI λ5876 lines. A similar phenomenon is encountered in some other AM Her-type representatives, for example, in FL Cet (Schmidt et al. 2005), V808 Aur (Borisov et al. 2016), and ZTFJ0850+0443 (Rodriguez et al. 2023). This effect is interpreted by the obscuration of the accretion spot by the optically thick part of the accretion stream. The phenomenon is apparently typical for systems with a high orbital inclination to which J1845 also

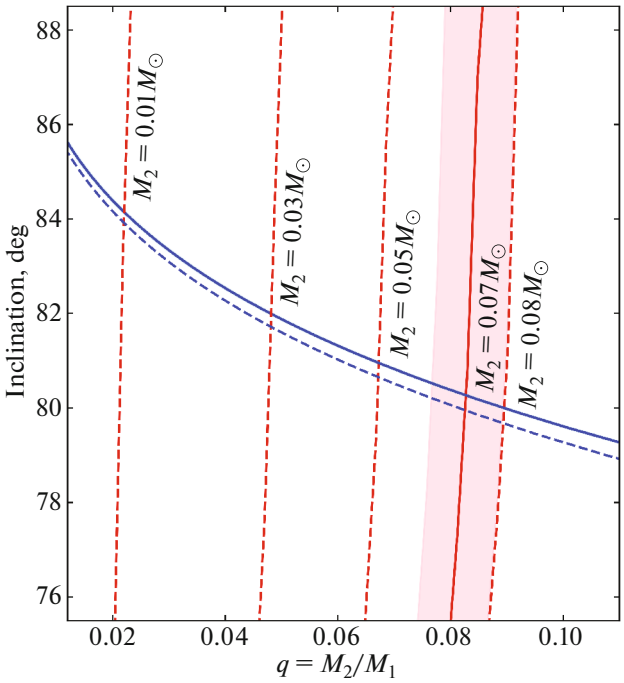

Fig. 6. Sets of solutions in the $q-i$ plane. The solid blue line indicates the solution that provides the observed duration of the eclipse if it were caused by the obscuration of an unspotted white dwarf by the donor. The dashed blue line corresponding to the limiting deviation from the first solution caused by the eclipse of a bright accretion spot. The solid red line is the solution that reproduces the radial velocity curve of the narrow Hα component for the donor mass $M_2 = 0.07\ M_\odot$. The dashed lines indicate analogous solutions for donors with masses of 0.08, 0.05, 0.03, and 0.01 $M_\odot$.

belongs. Note also that, in contrast to the presented examples of systems with line inversions, no pre-eclipse dip is detected in the light curves of J1845. The part of the stream J1845 obscuring the accretion spot is probably optically thin in continuum, which can be caused by a lower accretion rate or geometric peculiarities in the orientation of the accretion flow toward the observer.

5. ESTIMATION OF THE SYSTEM PARAMETERS

The existence of a white dwarf eclipse in cataclysmic variables makes it possible to impose constraints on the masses of the system components and the orbital inclination. Since the donor fills its Roche lobe, the duration of the accretor eclipse is determined by the mass ratio $q = M_2/M_1$ and the orbital inclination i (Horne 1985). The solution in the $q - i$ plane that provides the observed eclipse duration $\Delta t_{\rm ecl} = 96.5 \pm 1.7$ s is shown in Fig. 6. It was constructed by assuming that the white dwarf center is obscured by the donor. The error in the eclipse duration gives an uncertainty in the orbital inclination of only $\sim 0.01^\circ$ in the range $q \in 0.02-0.10$. The absence of coordinates of the source being eclipsed introduces a greater uncertainty into the solution. As we assumed in Section 3, the observed eclipse in J1845 results from the obscuration of a small part of the white dwarf disk containing a bright accretion spot by the donor. In the same figure we superimposed the solution that corresponds to the eclipse of a point on the white dwarf surface facing the donor. In our calculations we used a white dwarf radius close to the maximum one and corresponding to the mass $M = 0.5\ M_\odot$, i.e., a mass close to the minimum one for cataclysmic variables (Zorotovic et al. 2011). Thus, the two constructed curves in the $q - i$ plane form the region in which the true solution for J1845 is located.

To further constrain the parameters, we used the radial velocity curve of the narrow Hα component. In the previous section we showed that it is most likely formed in the accretion stream near the Lagrange point L_1. In that case, it can be assumed that the formation region of the narrow component is located at a fairly large distance from the threading region, where the gas motion is not distorted by the white dwarf magnetic field and occurs along a trajectory close to the ballistic one. The observed radial velocity semi-amplitude of the narrow component K_n and its initial phase φ_n^0 are functions of four parameters: the orbital inclination i, the mass ratio q, the secondary mass M_2, and the distance of the emission formation region from the Lagrange point L_1. Obviously, an additional relation to remove the uncertainty in the mass M_2 will be required to construct the solution in the $q - i$ plane corresponding to the observed K_n and φ_n^0. Such a relation is often constructed based on the filling by the donor of its Roche lobe whose effective radius is defined as

$$R_L = A\frac{0.5126q^{0.7388}}{0.6710q^{0.7349} + \ln(1 + q^{0.3983})}, \qquad (4)$$

where A is the semimajor axis of the system related to the component masses and the orbital period via Kepler's third law $A = (M_2(1 + 1/q)P_{\rm orb}^2)^{1/3}$. Formula (4) is valid for fully convective stars (Sirotkin and Kim 2009; Knigge et al. 2011) described by polytropic models with the index $n = 3/2$. The donor mass–Roche lobe radius relation constructed for white dwarf masses $M_1 = 0.5 - 1.44\ M_\odot$ is shown in Fig. 7. The same figure shows the empirical donor mass–radius relation from Knigge et al. (2011). It can be seen that there is no intersection of the curves $R_L(M_2)$ and $R_2(M_2)$, but there is agreement between the radii within the error limits for $M_2 < 0.08\ M_\odot$. Since the system has a very short orbital period for cataclysmic variables, we deem the donor mass $M_2 = 0.07\ M_\odot$ that corresponds to the turn of the

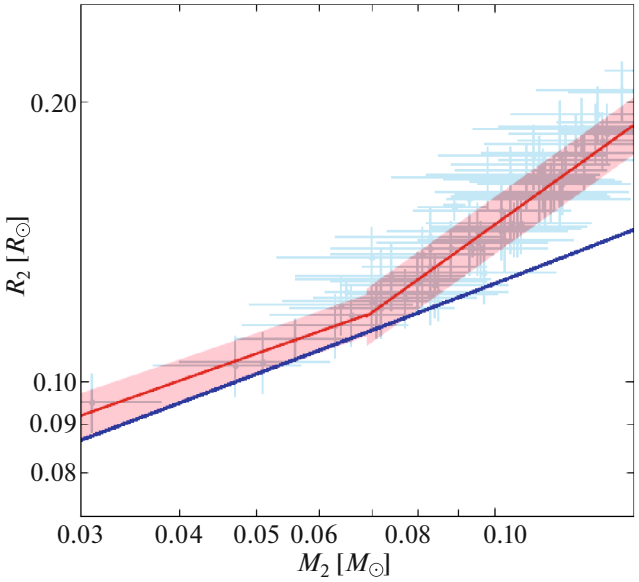

Fig. 7. Mass–radius relation for the donor in cataclysmic variables. The points with error bars correspond to the donor mass and radius measurements taken from Knigge (2006). The lines indicate the power-law fits for donors with masses $M_2 < 0.069\ M_\odot$ (the so-called bouncers) and $0.069\ M_\odot < M_2 < 0.20\ M_\odot$ obtained by Knigge (2006) and Knigge et al. (2011). The blue lines indicate the effective radii of the donor's Roche lobe calculated for white dwarf masses $M_1 \in 0.50-1.44\ M_\odot$.

system's evolution from a decreasing period to an increasing one to be the most probable.

On the $q - i$ plane shown in Fig. 6 we superimposed the solutions consistent with the assumption that the narrow Hα component is formed on the ballistic trajectory for donor masses of 0.08, 0.05, 0.03, and 0.01 $M_\odot$. The ballistic trajectory was calculated by solving the restricted three-body problem (Flannery 1975). The curve corresponding to the mass $M_2 = 0.08\ M_\odot$ gives the constraints on the mass ratio $q \le 0.09$, the white dwarf mass $M_1 \le 0.89\ M_\odot$, and the orbital inclination $i \ge 79.7°$. The curve calculated for the mass $M_2 = 0.01\ M_\odot$ close to the minimum mass of brown dwarfs gives another constraint on the parameters. The constraints on the white dwarf mass $M_1 \ge 0.49\ M_\odot$ and the orbital inclination $i \le 84.3°$ follow from it.

Figure 6 also shows the solution for, as we think, the most probable donor mass $M_2 = 0.07\ M_\odot$ used below to model the polarization observations. The mass ratio $q = 0.083$, the white dwarf mass $M_1 = 0.85 \pm 0.07\ M_\odot$, and the orbital inclination $i = 80° \pm 0.5°$ correspond to it. When calculating the errors in these parameters, we took into account the errors in K_n and φ_n^0.

6. CYCLOTRON SPECTRA

Weak cyclotron harmonics are observed in the spectra of J1845 during the entire orbital period. We analyzed them based on the September 21/22, 2011 spectra taken in the widest spectral range. These spectra exhibit three harmonics near wavelengths of 5100, 5900, and 6700 Å that are most pronounced in the bright phase. A difference by ≈150–300 Å in the wavelengths of the harmonics in the bright and dim phases is noticeable, but no variability in the positions of the harmonics within the brightness phase is detected. The spectra with the most pronounced harmonics from the bright and dim phases corresponding to the orbital phases $\varphi = 0.81$ and 0.26 are presented in Fig. 8. We modeled them using the simple model of an accretion spot homogeneous in temperature and density. Within this model the intensities of the emergent radiation in the ordinary (o) and extraordinary (e) modes are defined as

$$I_{o,e} = I_{RJ}[1 - \exp(-\alpha_{o,e}\Lambda)], \qquad (5)$$

where $I_{RJ} = k_B T\omega^2/8\pi^3c^2$ is the Rayleigh–Jeans intensity per polarization mode, $\alpha_{o,e}$ are the cyclotron absorption coefficients in units of $\omega_p^2/\omega_c c$ for the ordinary and extraordinary waves (ω_p is the plasma frequency, ω_c is the cyclotron frequency), and $\Lambda = \omega_p^2\ell/\omega_c c$ is the plasma parameter dependent on the thickness of the emitting region along the line of sight ℓ. The absorption coefficients $\alpha_{o,e}$ depend on the radiation frequency, the temperature of the emitting medium, and the angle between the magnetic field lines and the line of sight. They were calculated by the method of Chanmugam and Dulk (1981). The total intensity of the cyclotron radiation is defined as the sum of the intensities of the ordinary and extraordinary waves, i.e., $I_{\rm cyc} = I_o + I_e$. The shape of the cyclotron spectrum depends on the magnetic field strength B, the electron temperature T_e, the plasma parameter Λ, and the angle θ between the magnetic field lines and the line of sight.

The parameters of the accretion spots were determined by the least-squares method. We failed to achieve a satisfactory description of the spectrum for the bright phase in a wide range of model parameters. We assumed that the main accretion spot has a two-component structure including the part with a spectrum close to the Rayleigh–Jeans one and the component whose spectrum contains cyclotron harmonics. The first component can be a dense or hot core whose spectrum degenerates into the Rayleigh–Jeans spectrum at a high optical depth $\tau_{o,e} = \alpha_{o,e}\Lambda$. The second component can be the periphery of the spot with a lower local accretion rate. The presence of

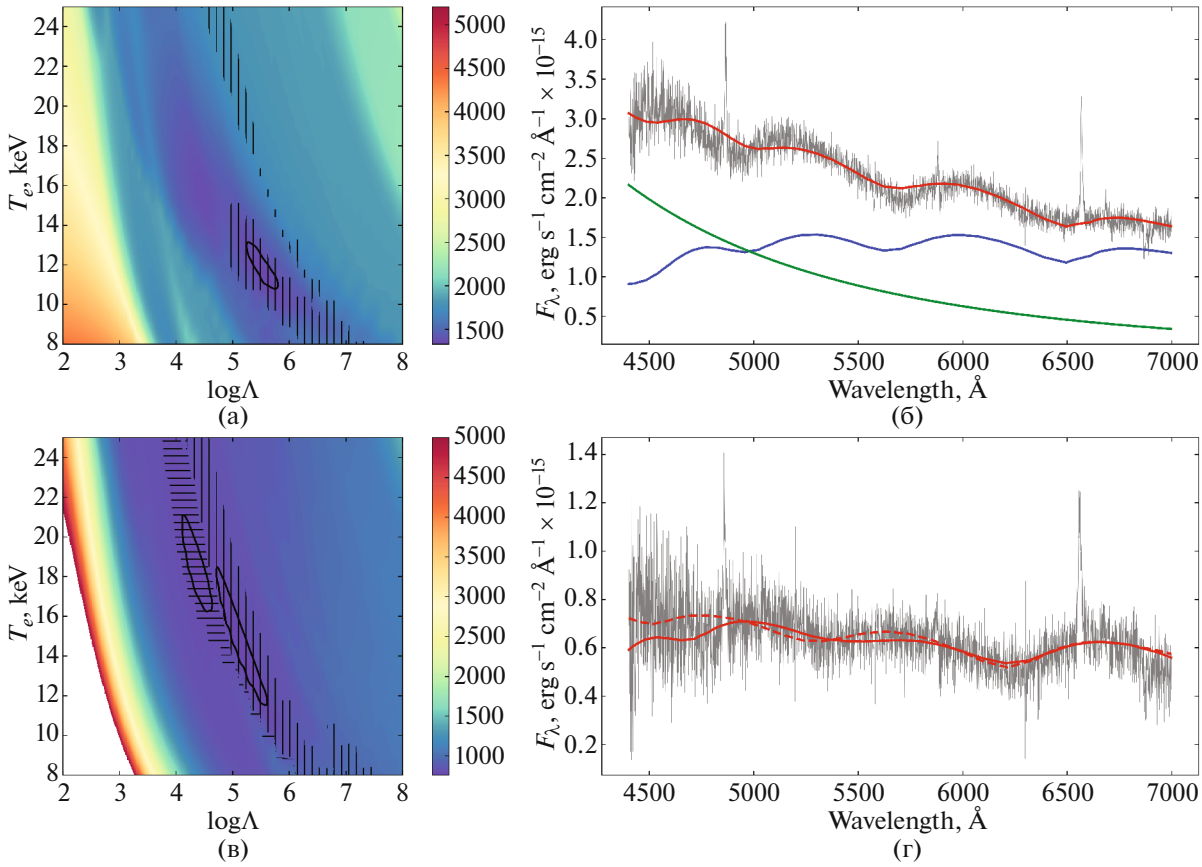

Fig. 8. Maps of the distribution of minimum χ^2 in the $\log\Lambda - T_e$ plane for the bright ($\varphi = 0.81$, panel (a)) and dim ($\varphi = 0.26$, panel (c)) phases. Panels (b) and (d) show the spectra of J1845 (gray line) and their fit (red line) for the bright and dim phases, respectively. For the bright phase the fitting spectrum is the sum of the cyclotron spectrum for a magnetic field $B = 28.4$ MG (blue line) and the Rayleigh–Jeans distribution (green line). The spectrum for the dim phase is described by the cyclotron spectra for magnetic fields $B = 30.3$ (solid red line) and 35.9 MG (dashed red line).

a dense structure is suggested by the weak polarization of J1845 in the bright phase (see the next section) that can also be associated with the high optical depth of the emitting region. The spectra were summed using the formula

$$F_\lambda = c\left(f\frac{1}{\lambda^4} + (1-f)I_{\rm cyc}\right), \qquad (6)$$

where c is the scale factor needed to convert the intensities to the observed fluxes and f regulates the contribution of the Rayleigh–Jeans component ($\sim 1/\lambda^4$) and the cyclotron component to the total spectrum ($0 \le f \le 1$). We sought the parameter f at fixed B, T_e, Λ, and θ by the golden section method. Note that it is not always possible to find the contribution of the components ($\sim cf$ and $\sim c(1-f)$) to the total radiation by solving the system of normal equations due to the possibility of negative solutions.

In contrast to the bright phase, the spectrum for the dim phase was described only by the cyclotron spectrum. The contribution of the white dwarf in the spectra being modeled must be small. For example, the state of the polar can be judged from its photometry performed with BTA/SCORPIO-2 immediately before the spectroscopic observations. The two brightness measurements obtained fall nicely on the light curve in the high state (see Fig. 9). Since the brightnesses at the phases under consideration in the high and low states differ by 2 mag, the contribution of the white dwarf radiation must be less than $\sim 1/5$ of the system's total radiation.

Figures 8a and 8c present maps of the distribution of optimal χ^2 in the $\log\Lambda - T_e$ plane for the spectra of the bright and dim phases, respectively. For each pair ($\log\Lambda$, T_e) of the presented maps the minimum χ^2 value is shown for the magnetic field B and angle θ. The isolines indicate the 99% confidence regions (see, e.g., Press et al. 2007). On the right graph the dashed lines indicate the region where the optimal magnetic field strength varies within the range 27–30 MG. It can be seen that this region captures completely the confidence interval from which we conclude that the magnetic field strength in the main accretion spot is

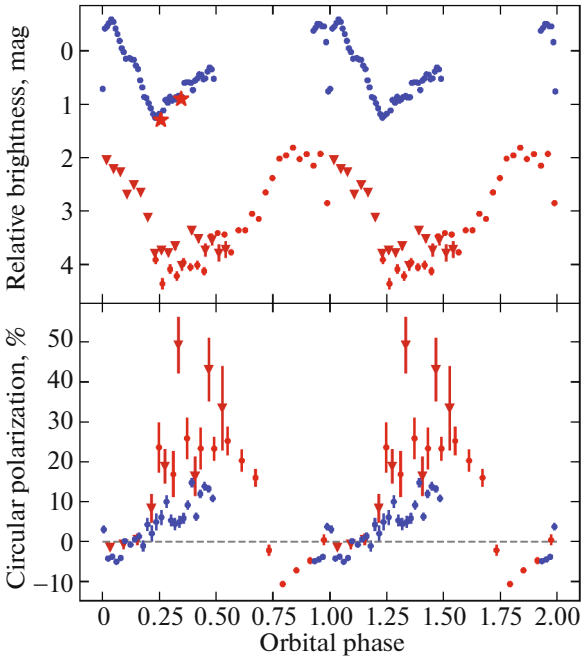

Fig. 9. Light curves (upper panels) and circular polarization curves (lower panel) for the polar J1845 in the V band. The blue and red markers indicate the August 28/29, 2011 and April 23/24, 2012 observations, respectively. The dots and triangles mark the observations for different cycles of the orbital period. The red stars represent the photometric data from the direct V images obtained before the September 21/22, 2011 spectroscopic observations.

$B = 28.4^{+0.1}_{-0.2}$ MG. The observed spectrum for this estimate of the magnetic field strength is described in Fig. 8b. On the χ^2 map for the dim phase there are two confidence regions covered by the optimal magnetic field strengths of 35–37 (horizontal dashes) and 29–34 MG (vertical dashes). Thus, for the second accretion spot there is an ambiguity in determining the magnetic field strength with its possible values of $B = 30.3^{+0.6}_{-0.4}$ and $35.9^{+0.8}_{-0.1}$ MG. The observed spectrum for two magnetic field estimates is described in Fig. 8d. Interestingly, for the two spectra being analyzed the optimal values of the angle θ are close (within 3°) to 90°. The accretion of gas probably occurs near the rotation poles, giving such values of the angle θ at an inclination of the rotation axis $i \approx 90°$. This assumption is also consistent with a weak variability in the positions of the cyclotron harmonics corresponding to a small change in the angle θ. In addition, this assumption made by analyzing the cyclotron spectra supports the hypothesis made in Section 3 that a small part of the white dwarf containing an accretion spot is eclipsed by the secondary.

7. POLARIMETRY

The light curves and circular polarization curves obtained with BTA/SCORPIO-2 in the V band are presented in Fig. 9. The dim phase with a weak photometric variability ($0.25 \lesssim \varphi \lesssim 0.70$) and the bright phase ($0.70 \lesssim \varphi \lesssim 1.25$), in which the system's brightness is enhanced by $\Delta V \approx 2\overset{\mathrm{m}}{.}5$, are traceable in the April 23/24, 2012 observations, just as in the ZTF and RTT-150 observations (see Section 3). The August 28/29, 2011 observations occurred at the polar's higher state differing in brightness from the April 23/24, 2012 state, on average, by $\Delta V \approx 1\overset{\mathrm{m}}{.}5$. In the high state the light curve has a more complex shape in which there is no plateau in the interval $0.25 \lesssim \varphi \lesssim 0.70$. A drop in the polarization amplitude from $V/I \in [-10, +30\%]$ to $V/I \in [-5, +10\%]$ during the transition from the low state to the high one is clearly seen. This phenomenon is expected for polars and is apparently caused by an increase in the optical depth of the accretion spots with an enhancement of the mass transfer and/or a great contribution of the continuum radiation from the accretion stream to the system's radiation in the high state (Schmidt et al. 2005; Romero-Colmenero et al. 2003).

The behavior of the circular polarization during the orbital period is of interest. First, there is a polarization sign reversal from negative in the bright phase to positive in the dim phase. Second, an anticorrelation of the polarization with the brightness of the polar can be seen. These phenomena are difficult to interpret in terms of the one-pole accretion model and, for this reason, we assume that there is accretion onto two magnetic poles in the polar. The main accreting pole gives the bright phase $0.70 \lesssim \varphi \lesssim 1.25$ and faces the donor, whereas weaker accretion near the opposite magnetic pole is observed at the plateau phase. The lower polarization of the radiation from the main accretion spot may be related to its greater optical depth. Note that the analysis of cyclotron spectra gives close magnetic field strengths in the two accretion spots, and the differences in polarization are unlikely to be caused by the difference of the magnetic fields. In addition, the system has a high inclination $i \approx 90°$ and, for this reason, the difference in the visibility conditions for the accretion spots also appears as a weak argument to explain the differences in polarization. Therefore, we consider the difference in the optical depths as the main hypothesis of the difference in polarization between the two accretion spots. The polarization sign reversal as the eclipse progresses (from $\approx -3.6\%$ near the eclipse to $\approx 4.0\%$ in the eclipse) detected in the August 28/29, 2011 observations engages our attention. This phenomenon is consistent with our assumption about a partial

eclipse of the white dwarf made in Section 3. Indeed, if the donor obscures only the "lower" part of the white dwarf with the main accretion spot, then the contribution from the vicinity of the second magnetic pole with an opposite polarization must increase in the system's total radiation.

The April 23/24, 2012 curves of the Stokes parameters I and V were modeled by the simple model of an accreting white dwarf with a dipole magnetic field proposed by Kolbin and Borisov (2020). In this model the accretion stream is described by two components: ballistic and magnetic. The particles move along the ballistic trajectory from the Lagrange point L_1 to the threading region, where they are captured by the white dwarf magnetic field. The position and size of the threading region are specified by the azimuthal angle α measured from the direction to the secondary and the azimuthal extent $\Delta\alpha$. After the threading region, the accretion stream material moves along magnetic field lines and settles near the white dwarf magnetic poles to form arc-shaped accretion spots. Just as in our modeling of the cyclotron spectra, the spots were assumed to be homogeneous in temperature and density, while their radiation spectrum was characterized by the electron temperature T_e, the dimensionless plasma parameter Λ, the magnetic field strength B, and the angle between the magnetic field lines and the line of sight θ. By calculating the convolution of the polarized radiation spectrum with the photometric filter transmission function, we computed a grid of the Stokes parameters I and V in the V band. This grid was interpolated when synthesizing the curves of the Stokes parameters for the system. For details on the method of modeling the light curves and polarization of polars, see Kolbin and Borisov (2020).

When modeling the observed Stokes parameters, we searched for the magnetic dipole orientation and the positions of the accretion spots on the white dwarf surface. The magnetic dipole orientation was specified by two angles: the inclination of the dipole axis to the rotation axis β and the longitude of the magnetic pole ψ measured from the direction to the donor's center of mass. The positions of the spots on the white dwarf surface were determined via the position of the threading region characterized by the angles α and $\Delta\alpha$. In accordance with the results of our modeling of the cyclotron spectra, the temperature of the accretion spots was fixed at 10 keV, while the magnetic field in the spots was taken to be 30 MG. The orbital inclination was set equal to $i = 80°$, while the masses of the white dwarf and the donor needed to calculate the ballistic trajectory were fixed at $M_1 = 0.85\ M_\odot$ and $M_2 = 0.07\ M_\odot$, respectively (see Section 5). We searched for the magnetic dipole orientation and the position of the threading region

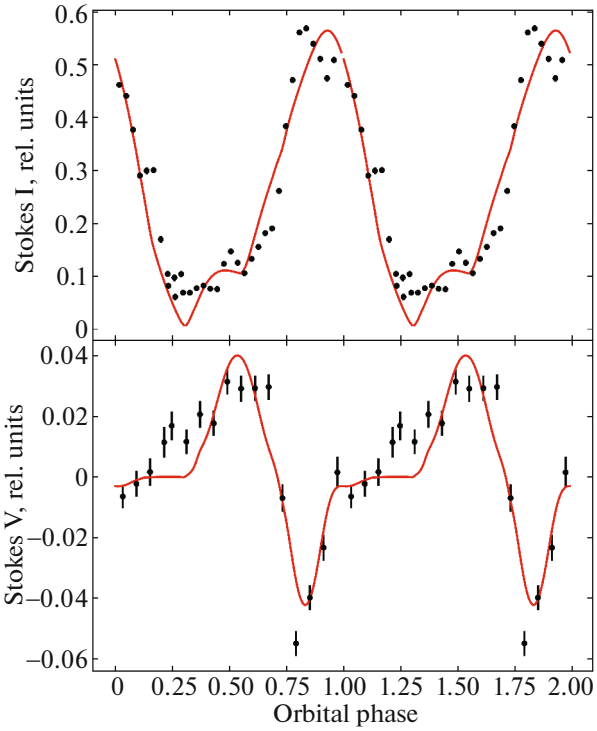

Fig. 10. The observed curves of the Stokes parameters I (black dots, upper panel) and V (black dots, lower panel) for the polar J1845 and their theoretical fits (red lines).

by minimizing χ^2 using the genetic algorithm. Our model of accretion in J1845 is visualized in Fig. 11. The magnetic dipole is inclined to the rotation axis by $\beta = 149°$ and the longitude of the magnetic pole is $\psi = 20°$. The main accretion spot is located in the lower, i.e., facing away from the observer, white dwarf hemisphere bounded by the equator. There is accretion onto it from the threading region that begins at the azimuthal angle $\alpha = 96°$ and has the extent $\Delta\alpha = 160°$. The capture of the gas by the magnetic field lines of the second spot begins from $\alpha = 89°$ and extends over $\Delta\alpha = 58°$. The plasma parameter for the first and second spots is $\log\Lambda = 7.0$ and 5.9, respectively. The observed light and polarization curves are compared with the model ones in Fig. 10. We see the qualitative description of the observations supporting our hypothesis about two-pole accretion with differing optical depths of the accretion spots. Given that the physical conditions in the two accretion spots are close, the ratio of the optical depths is estimated to be $\tau_1/\tau_2 \approx \Lambda_1/\Lambda_2 \approx 10$.

8. SWIFT OBSERVATIONS

The X-ray spectrum of J1845 was taken with XRT of the Swift orbital observatory. The emission was recorded in the energy range $E = 0.2–10$ keV with an accumulation time of 11.5 ks (ObsID 00031970).

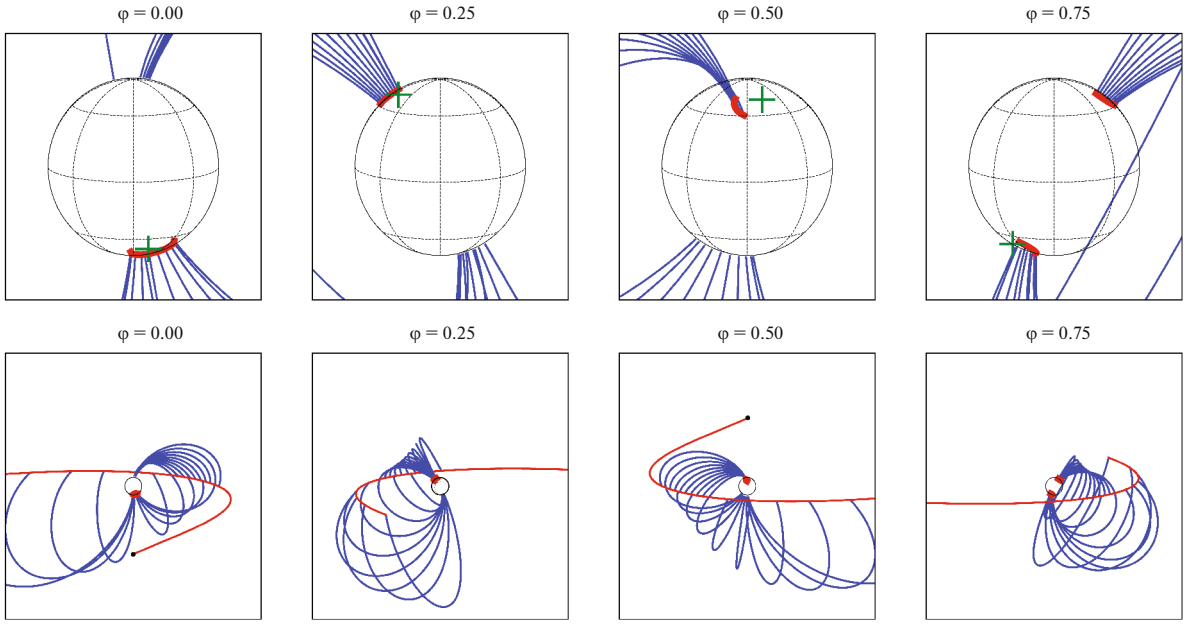

Fig. 11. The model of the polar J1845 optimally consistent with the polarization observations. The upper panels show the models of the J1845 white dwarf at different orbital phases φ. The red lines indicate the accretion spots; the blue lines indicate the magnetic dipole lines emerging from the accretion spots. The green crosses indicate the positions of the magnetic poles. The same models are shown on the lower panels with a larger field of view. The red line indicates the ballistic trajectory of the particles escaping from the Lagrange point L_1.

The spectrum was extracted using the online Swift/XRT data extraction service[4] (Evans et al. 2009). To analyze the spectral observations, we used the Xspec code from the HEASoft package.[5] The spectrum was binned in such a way that there were at least six counts per spectral channel.

Two main components exist in the X-ray spectra of polars: the accretion spot bremsstrahlung and the part of the white dwarf surface heated by the accretion spot radiation having a Planck spectrum with its maximum in the soft X-ray band (Cropper 1990). We fitted the spectrum of J1845 by the bremsstrahlung spectrum with absorption (the tbabs(bremss) model in Xspec) and the blackbody spectrum with absorption (the tbabs(bbody) model). The chemical composition from Wilms et al. (2000) was used in the tbabs absorption model. The color excess from the maps by Schlafly and Finkbeiner (2011) toward J1845 is $E(B-V) = 0^{\rm m}.0538 \pm 0^{\rm m}.0009$.[6] Since the maps by Schlafly and Finkbeiner (2011) give the Galactic extinction, the estimate of the color excess obtained is an upper limit for this parameter. The parallax of J1845 from the Gaia DR3 catalogue $p'' = (-0.336 \pm 0.980) \times 10^{-3}$ gives the constraint on the distance $D \gtrsim 1500$ пк (Gaia Collaboration 2020). The three-dimensional (3D) extinction maps by Lallement et al. (2014) and Capitanio et al. (2017) are limited toward J1845 by a distance of 830 pc and give a lower limit for the color excess $E(B-V) = 0^{\rm m}.037 \pm 0^{\rm m}.015$.[7] Extrapolation of these maps to $D = 1500$ pc gives $E(B-V) \approx 0^{\rm m}.051$. Based on the 3D interstellar extinction maps by Green et al. (2019),[8] the color excess is found to be $E(g-r) = 0^{\rm m}.05 \pm 0^{\rm m}.02$ or $E(B-V) = 0^{\rm m}.048 \pm 0^{\rm m}.019$ (Fukugita et al. 1996). Taking into account the estimates of the color excess found, we adopted $E(B-V) = 0^{\rm m}.052 \pm 0^{\rm m}.002$ and the extinction $A_V = 3.1E(B-V) = 0^{\rm m}.16 \pm 0^{\rm m}.06$. Using the empirical relation from Foight et al. (2016) with our A_V estimate, we obtained the hydrogen column density $N_H = (0.46 \pm 0.17) \times 10^{21}$ cm^{-2}.

Because of the small number of recorded photons, the spectrum of J1845 was fitted using the C-statistic (Cash 1979). The best fit to the spectrum by the blackbody model is achieved at the temperature $T =$

[4] The Swift/XRT observational data extraction service is accessible at https://www.swift.ac.uk/user_objects/.

[5] The HEASoft software package is accessible at https://heasarc.gsfc.nasa.gov/lheasoft/.

[6] The service on determining the interstellar extinction from the maps by Schlafly and Finkbeiner (2011) is accessible at https://irsa.ipac.caltech.edu/applications/DUST/.

[7] The service for work with the 3D interstellar extinction maps by Lallement et al. (2014) is accessible at https://stilism.obspm.fr/.

[8] The service for work with the 3D interstellar extinction maps by Green et al. (2019) is accessible at http://argonaut.skymaps.info/.

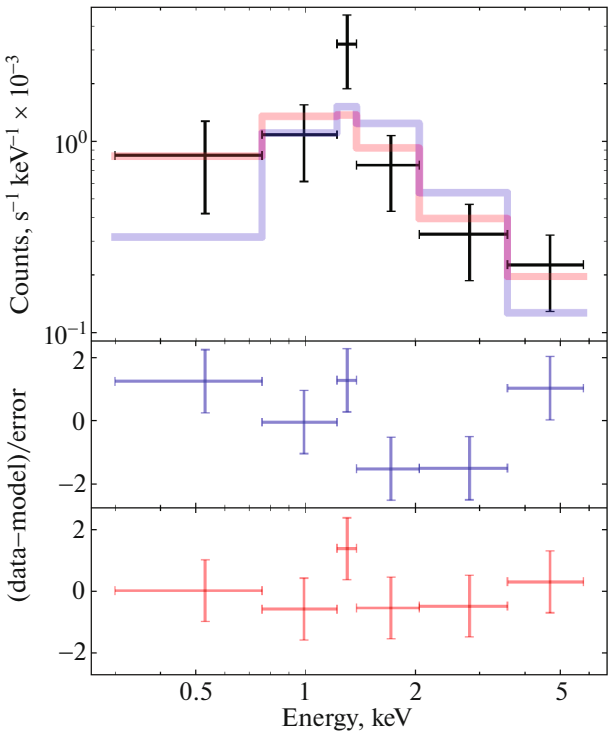

Fig. 12. Upper panel: the X-ray spectrum of J1845 (the black error bars along both axes) described by the blackbody (blue line) and bremsstrahlung (red line) models. The lower panels show the weighted residuals for the blackbody (blue error bars) and bremsstrahlung (red error bars) spectra.

0.72 ± 0.09 keV ($C = 9.88$, $\nu = 4$) and is presented in Fig. 12. The best reproduction of the spectrum can be achieved with the bremsstrahlung model ($C = 4.03$, $\nu = 4$) also shown in Fig. 12. However, using this model does not allow the temperature to be determined because of the low accumulation of X-ray photons. According to the Akaike (1974) criterion, the accretion spot bremsstrahlung is the more probable main X-ray source. We estimated the X-ray flux $F_X \approx 1.3 \times 10^{-13}$ erg cm^{-2} s^{-1} in the $0.2 - 5.5$ keV band by integrating the flux in the bremsstrahlung model. Given the available constraint on the distance to J1845, we have an X-ray luminosity of the polar $L_X \gtrsim 3.5 \times 10^{31}$ erg s^{-1}.

The polar J1845 was also observed from May 1 to 2, 2011, with the ultraviolet/optical Swift/UVOT telescope in the $UVW1$ band (1500–3500 Å). During ≈0.8 day 52 frames were taken with exposure times of 196.6 s. Aperture photometry for J1845 was performed using the uvotmaghist code from the HEASoft package. Figure 1 presents the ultraviolet phased light curve constructed using the ephemeris (1). The error in the orbital phases is $\Delta\varphi = 0.03$. A comparison of the Swift/UVOT light curve with the ZTF light curve shows a correlation between the optical and ultraviolet fluxes pointing to the formation of ultraviolet radiation in the accretion spots or in their vicinity. The ultraviolet light curve has a bright phase in the range $0.80 \lesssim \varphi \lesssim 1.20$ and a dim phase near $0.25 \lesssim \varphi \lesssim 0.75$, the amplitude of the brightness variations is $\Delta UVW1 \approx 1\overset{\mathrm{m}}{.}1$.

CONCLUSIONS

In this paper we carried out a comprehensive study of the eclipsing polar J1845. It included the analysis of long-term ZTF photometry, fast RTT-150 photometry, BTA/SCORPIO-1/2 phase-resolved spectroscopy, BTA/SCORPIO-2 phase-resolved polarimetry, Swift/UVOT ultraviolet photometry, and Swift/XRT X-ray observations. Below we list our main results.

High and low states of J1845 differing in maximum brightness by $\Delta r \approx 1\overset{\mathrm{m}}{.}5$ manifest themselves in the long-term ZTF observations. A dim phase with a small change in brightness spanning approximately half the orbital period ($0.25 \lesssim \varphi \lesssim 0.70$) and a bright phase ($0.70 \lesssim \varphi \lesssim 1.25$) formed by the passage of the main accretion spot across the white dwarf disk manifest themselves in the phased light curves. A shift of the bright phase and its extension corresponding to a change in the longitude of the accretion spot by ≈25° and its extension in longitude over ≈43° are observed during the transition from the low state to the high one. An eclipse with a duration $\Delta t_{\mathrm{ecl}} = 96.5 \pm 1.7$ s is observed, which is apparently the obscuration of a small part of the white dwarf disk with an accretion spot by the donor.

Narrow and broad components with radial velocity semi-amplitudes $K_n = 503 \pm 9$ km s^{-1} and $K_b = 447 \pm 12$ km s^{-1}, respectively, manifest themselves in the dynamic Hα spectra. An analysis of the Doppler maps points to the formation of the narrow component not far from the Lagrange point L_1, whereas the broad component is most likely formed on the magnetic trajectory of the accretion stream. Near an orbital phase $\varphi \approx 0.85$ there is an inversion of the emission profile to the absorption one and back. This phenomenon is widespread among polars with a high orbital inclination and is apparently caused by the obscuration of the accretion spot by an optically thick accretion stream.

From the measured eclipse duration and the assumption about the formation of the narrow component of spectral lines on the ballistic trajectory we imposed constraints on the orbital inclination, $79.7° \leq i \leq 84.3°$, and the white dwarf mass, $0.49 \leq M_1/M_\odot \leq 0.89$. The parameters were constrained under the assumption of a secondary mass from the range $0.01 \leq M_2/M_\odot \leq 0.08$. The upper limit for

M_2 was determined from the empirical mass–radius relation for the donors in cataclysmic variables and the requirement for the donor to fill its Roche lobe, while the lower limit for M_2 is close to the minimum mass of a brown dwarf.

Cyclotron harmonics were observed in the spectra of J1845 over the entire orbital period. The positions of the harmonics in the dim and bright phases differ by 150–300 Å apparently due to the observation of different accretion spots: the main accretion spot in the bright phase and the secondary spot in the dim phase. A two-component model including the Rayleigh–Jeans spectrum and the cyclotron spectrum was required to be introduced to describe the spectrum for the bright phase. We found the magnetic field strength in the main accretion spot, $B_1 = 28.4^{+0.1}_{-0.2}$ MG, and estimated the temperature of the source of cyclotron harmonics, $T \approx 12$ keV. Our modeling of the cyclotron spectrum for the dim phase gave two possible solutions with magnetic field strengths in the secondary spot $B_2 = 30.3^{+0.6}_{-0.4}$ MG and $35.9^{+0.8}_{-0.1}$ MG and a temperature from the range 12–20 keV.

The polarization observations of J1845 reveal a circular polarization sign reversal during the orbital period that confirms the two-pole accretion regime. The polarization anticorrelates with the brightness of the polar apparently due to the greater optical depth of the main accretion spot. A comparison of the observations performed in different states of the polar shows a decrease in the polarization amplitude from $V/I \in [-10, +30\%]$ to $V/I \in [-5, +10\%]$ during the transition from the low state to the high one. We modeled the light curve and the circular polarization curve using the simple model of a polar with two-pole accretion. Our modeling gives a satisfactory description of the polarization observations supporting our assumption about two-pole accretion with a great difference (approximately by a factor of 10) in the optical depths of the accretion spots.

The X-ray spectrum of J1845 had a small accumulation. However, its modeling points to the formation of the bulk of the X-ray radiation in the accretion spot and not in the heated white dwarf photosphere. The constraint on the X-ray luminosity $L_X \gtrsim 3.5 \times 10^{31}$ erg s^{-1} is consistent with the X-ray luminosity of AM Her systems. The ultraviolet light curve of J1845 correlates with the optical behavior of its brightness, suggesting the formation of ultraviolet radiation in or near the accretion spots.

ACKNOWLEDGMENTS

We are grateful to TÜBİTAK, the Space Research Institute of the Russian Academy of Sciences, the Kazan Federal University, and the Academy of Sciences of Tatarstan for their partial support in using RTT-150 (the Russian–Turkish 1.5-m telescope in Antalya).

FUNDING

This study was supported by the Russian Science Foundation (project no. 22-72-10064). The observations with the telescopes at the Special Astrophysical Observatory of the Russian Academy of Sciences are supported by the Ministry of Science and Higher Education of the Russian Federation. The instrumentation is updated within the "Science and universities" National Project.

CONFLICT OF INTEREST

The authors of this work declare that they have no conflicts of interest.

REFERENCES

1. V. L. Afanasiev and V. R. Amirkhanyan, Astrophys. Bull. **67**, 438 (2012).
2. V. L. Afanasiev and A. V. Moiseev, Baltic Astron. **20**, 363 (2011).
3. K. Aizu, Prog. Theor. Exp. Phys. **49**, 1184 (1973).
4. H. Akaike, IEEE Trans. Autom. Control **19**, 716 (1974).
5. D. Belloni, M. R. Schreiber, A. F. Pala, B. T. Gansicke, M. Zorotovic, and C. V. Rodrigues, Mon. Not. R. Astron. Soc. **491**, 5717 (2020).
6. R. Bohlin, L. Colina, and D. Finley, Astron. J. **110**, 1316 (1995).
7. J. M. Bonnet-Bidaud, M. Mouchet, C. Busschaert, E. Falize, and C. Michaut, Astron. Astrophys. **579**, A24 (2015).
8. N. V. Borisov, M. M. Gabdeev, and V. L. Afanasiev, Astrophys. Bull. **71**, 95 (2016a).
9. N. V. Borisov, M. M. Gabdeev, V. V. Shimansky, N. A. Katysheva, A. I. Kolbin, S. Yu. Shugarov, and V. P. Goranskij, Astrophys. Bull. **71**, 101 (2016b).
10. G. P. Briggs, L. Ferrario, C. A. Tout, and D. T. Wickramasinghe, Mon. Not. R. Astron. Soc. **481**, 3604 (2018).
11. C. Busschaert, É. Falize, C. Michaut, J.-M. Bonnet-Bidaud, and M. Mouchet, Astron. Astrophys. **579**, A25 (2015).
12. L. Capitanio, R. Lallement, J. L. Vergely, M. Elyajouri, and A. Monreal-Ibero, Astron. Astrophys. **606**, A65 (2017).
13. W. Cash, Astrophys. J. **228**, 939 (1979).
14. G. Chanmugam and G. A. Dulk, Astrophys. J. **244**, 569 (1981).
15. M. Cropper, Space Sci. Rev. **54**, 195 (1990).
16. D. V. Denisenko and K. V. Sokolovsky, Astron. Lett. **37**, 91 (2011).
17. P. G. van Dokkum, Publ. Astron. Soc. Pacif. **113**, 1420 (2001).

18. P. A. Evans, A. P. Beardmore, K. L. Page, J. P. Osborne, P. T. O'Brien, R. Willingale, R. L. C. Starling, D. N. Burrows, et al., Mon. Not. R. Astron. Soc. **397**, 1177 (2009).
19. L. Ferrario, D. de Martino, and B. Gänsicke, Space Sci. Rev. **191**, 111 (2015).
20. B. P. Flannery, Mon. Not. R. Astron. Soc. **170**, 325 (1975).
21. D. Foight, T. Güver, and F. Özel, Astrophys. J. **826**, 66 (2016).
22. M. Fukugita, T. Ichikawa, J. E. Gunn, M. Doi, K. Shimasaku, and D. P. Schneider, Astron. J. **111**, 1748 (1996).
23. GAIA Collab., VizieR Online Data Catalog Gaia EDR3 (2020).
24. G. M. Green, E. Schlafly, C. Zucker, J. S. Speagle, and D. Finkbeiner, Astrophys. J. **887**, 93 (2019).
25. J.-M. Hameury, A. R. King, and J.-P. Lasota, Mon. Not. R. Astron. Soc. **218**, 695 (1986).
26. F. V. Hessman, B. T. Gänsicke, and J. A. Mattei, Astron. Astrophys. **361**, 952 (2000).
27. K. Horne, Mon. Not. R. Astron. Soc. **213**, 129 (1985).
28. K. Horne, Publ. Astron. Soc. Pacif. **98**, 609 (1986).
29. C. Knigge, Mon. Not. R. Astron. Soc. **373**, 484 (2006).
30. C. Knigge, I. Baraffe, and J. Patterson, Astrophys. J. Suppl. Ser. **194**, 28 (2011).
31. A. I. Kolbin and N. V. Borisov, Astron. Lett. **46**, 812 (2020).
32. A. I. Kolbin, N. V. Borisov, N. A. Serebriakova, V. V. Shimansky, N. A. Katysheva, M. M. Gabdeev, and S. Yu. Shugarov, Mon. Not. R. Astron. Soc. **511**, 20 (2022).
33. A. I. Kolbin, N. V. Borisov, A. N. Burenkov, O. I. Spiridonova, I. F. Bikmaev, and M. V. Suslikov, Astron. Lett. **49**, 129 (2023).
34. E. J. Kotze, S. B. Potter, and V. A. McBride, Astron. Astrophys. **579**, 77 (2015).
35. E. J. Kotze, S. B. Potter, and V. A. McBride, Astron. Astrophys. **595**, 47 (2016).
36. R. Lallement, J.-L. Vergely, B. Valette, et al., Astron. Astrophys. **561**, A91 (2014).
37. J. Li, ASP Conf. Ser. **157**, 235 (1999).
38. Y. Liu, H.-C. Hwang, N. L. Zakamska, and J. R. Thorstensen, Mon. Not. R. Astron. Soc. **522**, 2719 (2023).
39. T. Marsh, Astrophys. Space Sci. **296**, 403 (2005).
40. F. Masci, R. Laher, B. Rusholme, et al., Publ. Astron. Soc. Pacif. **131**, 995 (2019).
41. M. McAllister, S. P. Littlefair, S. G. Parsons, V. S. Dhillon, T. R. Marsh, B. T. Gansicke, E. Breedt, C. Copperwheat, et al., Mon. Not. R. Astron. Soc. **486**, 5535 (2019).
42. J. B. Oke, Astron. J. **99**, 1621 (1990).
43. E. Pavlenko, K. Sokolovsky, A. Baklanov, K. Antonyuk, O. Antonyuk, and D. Denisenko, Astron. Telegram **3436**, 1 (2011).
44. J. T. van der Plas, Astrophys. J. Suppl. Ser. **236**, 16 (2018).
45. W. H. Press, S. A. Teukolsky, W. T. Vetterling, et al., *Numerical Recipes. The Art of Scientific Computing,* 3rd ed. (Cambridge Univ. Press, Cambridge, 2007).
46. H. Ritter and U. Kolb, Astron. Astrophys. **404**, 301 (2003).
47. A. Rodriguez, S. Kulkarni, T. Prince, P. Szkody, K. B. Burdge, I. Caiazzo, J. van Roestel, Z. P. Vanderbosch, et al., Astrophys. J. **945**, 141 (2023).
48. E. Romero-Colmenero, S. B. Potter, D. A. H. Buckley, P. E. Barrett, and S. Vrielmann, Mon. Not. R. Astron. Soc. **339**, 685 (2003).
49. Th. Rousseau, A. Fischer, K. Beuermann, and U. Woelk, Astron. Astrophys. **310**, 526 (1996).
50. E. Schlafly and D. Finkbeiner, Astrophys. J. **737**, 103 (2011).
51. G. Schmidt, P. Szkody, L. Homer, P. S. Smith, B. Chen, A. Henden, J.-E. Solheim, M. A. Wolfe, and R. Greimel, Astrophys. J. **620**, 422 (2005).
52. A. D. Schwope, K. H. Mantel, and K. Horne, Astron. Astrophys. **319**, 894 (1997).
53. A. D. Schwope, F. Mackebrandt, B. D. Thinius, C. Littlefield, P. Garnavich, A. Oksanen, and T. Granzer, Astron. Nachr. **336**, 115 (2015).
54. F. Sirotkin and W.-T. Kim, Astrophys. J. **698**, 715 (2009).
55. D. Steeghs, Mon. Not. R. Astron. Soc. **344**, 448 (2003).
56. S. Tapia, Astrophys. J. Lett. **212**, L125 (1977).
57. B. Warner, *Cataclysmic Variable Stars* (Cambridge Univ. Press, Cambridge, 1995).
58. J. Wilms, A. Allen, and R. McCray, Astrophys. J. **542**, 914 (2000).
59. H. Worpel and A. D. Schwope, Astron. Astrophys. **583**, A130 (2015).
60. M. Zorotovic, M. R. Schreiber, and B. T. Gänsicke, Astron. Astrophys. **536**, 42 (2011).

Translated by V. Astakhov